

# Combining Spiral Scanning and Internal Model Control for Sequential AFM Imaging at Video Rate

Ali Bazaei, *Member, IEEE*, Yuen Kuan Yong, *Member, IEEE*, and S. O. Reza Moheimani, *Fellow, IEEE*

**Abstract**—We report on the application of internal model control for accurate tracking of a spiral trajectory for atomic force microscopy (AFM). With a closed-loop bandwidth of only 300 Hz, we achieved tracking errors as low as 0.31% of the scan diameter and an ultravideo frame rate for a high pitch (30 nm) spiral trajectory generated by amplitude modulation of 3 kHz sinusoids. Design and synthesis procedures are proposed for a smooth modulating waveform to minimize the steady-state tracking error during sequential imaging. To obtain AFM images under the constant-force condition, a high bandwidth analogue proportional-integral controller is applied to the damped  $z$ -axis of a flexure nanopositioner. Efficacy of the proposed method was demonstrated by artifact-free images at a rate of 37.5 frames/s.

**Index Terms**—Atomic force microscopy (AFM) imaging, internal model control, nanopositioning, spiral scan, video rate.

## I. INTRODUCTION

THE DEMAND for video-rate atomic force microscopy (AFM) is increasing rapidly, particularly in fields that involve study of biological cells [1], high-throughput nanomachining [2] and nanofabrication [3]. Traditionally, raster-based trajectory has been the common type of scanning pattern used in the AFM [4]. The raster trajectory is constructed from a synchronized triangular waveform tracked by the fast axis of a nanopositioner; and a staircase or ramp signal tracked by the slow axis. The nanopositioner is a highly resonant structure with a finite mechanical bandwidth. Tracking of the fast triangular waveform, consisting of its fundamental frequency and all associated odd harmonics, tends to excite the resonance frequencies of the nanopositioner [5], [6]. One typical method to avoid the

Manuscript received August 27, 2015; revised February 18, 2016; accepted April 16, 2016. Date of publication June 1, 2016; date of current version February 14, 2017. Recommended by Technical Editor Q. Zou. This work was supported by the Australian Research Council and by the University of Newcastle Australia.

A. Bazaei and Y. K. Yong are with the School of Electrical Engineering and Computer Science, University of Newcastle Australia, Callaghan, NSW 2308, Australia (e-mail: Ali.Bazaei@newcastle.edu.au; Yuenkuan.Yong@newcastle.edu.au).

S. O. R. Moheimani is with the Department of Mechanical Engineering, University of Texas at Dallas, Richardson, TX 75080 USA (e-mail: Reza.Moheimani@utdallas.edu).

Color versions of one or more of the figures in this paper are available online at <http://ieeexplore.ieee.org>.

Digital Object Identifier 10.1109/TMECH.2016.2574892

excitation of these resonant modes is to scan at 1/100th to 1/10th of the dominant resonance frequency of the nanopositioner [7], which clearly limits the scan speed of the AFM.

Another approach to increasing the scan speed of the AFM is to employ a nonraster scan method. Cycloid [8] and Lissajous [6], [9], [10] scanning methods have been implemented successfully. Another viable nonraster scanning method is based on tracking a spiral trajectory [11]. In this method, sinusoidal reference signals with identical frequencies, but 90° phase difference, and time-varying amplitudes are employed for the two orthogonal axes of the scanner. In contrast to other nonraster scan methods, the spiral approach progressively covers new areas of the sample and has well-defined spacings between successive scan lines. The control approaches that have already been applied for spiral scanning include positive position feedback [11], [12], multi-input multi-output (MIMO) model predictive control [13], linear quadratic Gaussian [14], and phase-locked loop [15]. As the frequency of the sinusoids increases for high-speed AFM imaging, the tracking error becomes larger due to the limited closed-loop bandwidth of these methods. On the other hand, an internal model controller (IMC) designed for tracking of a constant amplitude sinusoid at a specific frequency can provide excellent asymptotic tracking and robust performance without imposing a high control bandwidth [6], [9]. Hence, it is desirable to synthesize IMC for spiral trajectories, where the sinusoidal reference amplitude varies with time. By internal model control, we mean including the dynamic modes of the reference and disturbance signals in the feedback controller while preserving the stability. Based on the internal model principle for linear time invariant systems, such a controller asymptotically regulates the tracking error to zero [16].

In this paper, we propose a novel application of IMC for tracking of spiral trajectories and demonstrate that this leads to significant control performance improvement. In contrast to the existing methods for spiral trajectory tracking, the proposed IMC controller can achieve zero steady-state tracking error, when the amplitude of the reference sinusoid changes linearly with time. The IMC controller also includes harmonics of the reference frequency to reduce the experimental tracking error arising from nonlinearities such as piezo actuator hysteresis and cross coupling. Furthermore, we propose a novel amplitude modulating waveform for spiral trajectory to considerably reduce the maximum magnitude of the tracking error during sequential imaging. The controller is implemented on the lateral

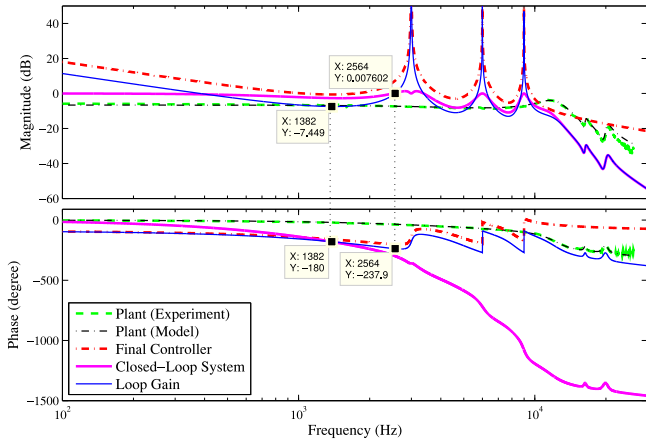


Fig. 1. Frequency responses of the  $y$ -axis after damping (plant). Also included are the final IMC (1), the closed-loop transfer function, and the loop gain for the  $y$ -axis.

axes of a state-of-the-art nanopositioner, embedded in a commercial scanning probe microscope for high-speed 3-D imaging. A high-bandwidth analogue controller is also implemented on the  $z$ -axis of the nanopositioner to conduct AFM imaging in constant-force contact-mode. Results of video-rate AFM imaging are presented and compared in both constant-height and constant-force modes.

The nanopositioner used in this paper is described in Section II. In Section III, we present the control design procedure for the proposed IMC. In Section IV, we discuss the tracking error problem, when spiral trajectory is periodically applied to the control system for sequential imaging. In this section, we also formulate a smooth modulating waveform for video-spiral trajectories and evaluate the tracking performance of the controller through simulation and experiments. Control design for  $z$ -axis and AFM imaging results are detailed in Sections V and VI, respectively.

## II. NANOPositionER

The  $x$ - $y$ - $z$  nanopositioning stage (scanner) is a flexible structure equipped with capacitive displacement sensors on  $x$ - and  $y$ -axes, piezoelectric strain sensors on the  $z$ -axis, and piezoelectric stack actuators that generate motion in three dimensions [17], [18]. The open-loop scanner has lightly damped resonant modes along each axis, which are required to be damped before the undamped modes of IMC controller can be implemented in a feedback system [6], [9]. The damping allows us to obtain a higher closed-loop bandwidth with adequate robustness to plant uncertainties and nonlinearities [19]. The lightly damped modes are effectively damped by integral resonant controllers (IRC) together with a passive dual mounted configuration for the  $z$ -axis, as described in [20] and [18]. For the lateral axes, the plant considered for control design is a model of the damped  $y$ -axis of the scanner, whose frequency response along with the experimental data are shown in Fig. 1. The model was obtained by manually assigning complex poles and zeros around the local peaks in the experimental data, in addition to real poles and zeros to include effects of delay and piezoelectric creep. The plant has a dc gain

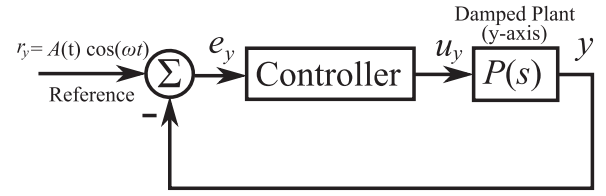


Fig. 2. Schematic of the control system for the  $y$ -axis. A similar control system is also used for the  $x$ -axis.

of 0.53 and the following poles and zeros:

$$\begin{aligned} \text{Poles} \\ -10^5 \left( \frac{\text{rad}}{\text{sec}} \right) &= 2.92, 1.81, 0.033 \pm 1.27i, 0.015 \pm 1.03i, \\ &0.11 \pm 0.76i, 0.31, 0.00022 \end{aligned}$$

$$\begin{aligned} \text{Zeros} \\ -10^5 \left( \frac{\text{rad}}{\text{sec}} \right) &= -2.86, 1.2, 0.03 \pm 1.23i, 0.013 \pm 1.02i, \\ &0.00025. \end{aligned}$$

## III. IMC FOR LATERAL AXES

The schematic of the control system for a lateral axis is shown in Fig. 2. To facilitate the design procedure, we assume that the final IMC  $C_f(s)$  is a linear combination of IMCs, each maintaining an acceptable closed-loop performance when used as the controller in the feedback loop depicted in Fig. 2, individually. That is,

$$C_f(s) = \sum_{k=0}^3 c_k C_k(s) \quad (1)$$

where the positive coefficients  $c_k$  corresponding to IMCs  $C_k(s)$  can be easily tuned, at a later stage. Each individual IMC contains the modes of a group of exogenous signals, which appear as a reference and/or disturbance in the system. Controller  $C_0(s) = \frac{K_i}{s}$  is an integrator. This controller has only one parameter that needs tuning and is included to cancel low frequency disturbances on the displacement output arising from nonlinearities and uncertainties such as cross-coupling, creep, and hysteresis. With an integral gain of  $K_i = 5000$ , the simulated control systems for both axes have settling times around 2 ms with gain and phase margins exceeding 27 dB and  $84^\circ$ , when  $C_0(s)$  is inserted as the controller in Fig. 2, individually.

Controller  $C_1(s)$  contains two pairs of purely imaginary poles at the fundamental frequency  $\omega = 6000 \pi \frac{\text{rad}}{\text{s}}$ , i.e., the frequency of the sinusoids that generate the spiral trajectory. The repeated imaginary poles in  $C_1(s)$  allow accurate tracking of sinusoidal references whose magnitudes vary linearly with time. In other words, the modes of such reference signals, which are presented by the repeated poles in the Laplace domain,<sup>11</sup> are to be included in the controller  $C_1(s)$ . The controller was designed based on  $H_\infty$  mixed-sensitivity synthesis method, which works with strictly stable weights. We selected

<sup>11</sup> $\mathcal{L}[t \cos(\omega t)] = \frac{(s^2 - \omega^2)}{(s^2 + \omega^2)^2}$ ,  $\mathcal{L}[t \sin(\omega t)] = \frac{2\omega s}{(s^2 + \omega^2)^2}$ .

a constant control weight  $W_2(s) = 5$  and a stable sensitivity weight  $W_1(s) = \left(1 + \frac{2\zeta s}{\omega} + \frac{s^2}{\omega^2}\right)^{-2}$  with a very small damping factor of  $\zeta = 10^{-4}$ . To enforce repeated poles in the controller close to the desired location, we also put an unstable filter  $F(s) = \left(1 - \frac{2\zeta s}{\omega} + \frac{s^2}{\omega^2}\right)^{-1}$  in series with the plant before inserting it in the optimization algorithm. Selecting these additional plant poles in the right-half-plane prevents any pole-zero cancellation of the desired poles in the resulting controller. The controller was then put in series with a filter similar to  $F(s)$  but stable. After reducing the order of the controller by applying model reduction to its balanced realization, the resulting IMC may be written as

$$C_1(s) = \frac{-0.2015 \left(1 - \frac{s}{2720}\right) \left(1 + \frac{2\zeta' s}{\omega'} + \frac{s^2}{\omega'^2}\right)}{\left(1 + \frac{s^2}{\omega^2}\right)^2} \quad (2)$$

where  $\zeta' = 0.0255$  and  $\omega' = 6005.4\pi$ . When individually inserted in the loop, the controller provides a settling time of 8 ms with stability margins around 20 dB and  $-63^\circ$  for both axes. The IMCs  $C_2(s)$  and  $C_3(s)$  in (1) are designed to cancel the second and the third harmonics of the reference frequency in the tracking error, respectively.

Due to the inherent plant nonlinearities such as hysteresis and creep, higher order harmonics of the reference frequency always appear in the tracking error. We can reduce the effect of a specific harmonic on the tracking error by incorporating an additional IMC with imaginary poles located at the harmonic frequency [9]. To obtain low-order controllers, we consider only one pair of imaginary poles for them, leaving only two parameters to be determined for each, i.e., a dc gain and a zero. As each controller is designed individually, tuning of the parameters is straightforward. The resulting controllers are as

$$C_2(s) = -0.455 \frac{1 - \frac{s}{105795}}{1 + \frac{s^2}{(2\omega)^2}} \quad (3)$$

$$C_3(s) = -0.471 \frac{1 + \frac{s}{282161}}{1 + \frac{s^2}{(3\omega)^2}} \quad (4)$$

When individually inserted in the loop, these controllers respectively provide settling times of 1.5 and 9 ms, while their stability margins are around 12 dB and  $\pm 80^\circ$  for  $y$ - and  $x$ -axes, respectively.

Having obtained IMCs with individually adequate closed-loop response and stability margins, we can easily tune their coefficients in (1) within a limited range of  $[0, 2]$ . With the coefficients  $c_0, \dots, c_3$  equal to 1, 2, 0.5, and 0.25, respectively, the final controller provides settling times less than 2 ms and stability margins around 7.4 dB and  $-58^\circ$  for both axes. The frequency response of the final IMC along with the closed-loop transfer function of the  $y$ -axis are also reported in Fig. 1. Considering a  $45^\circ$  phase lag, the closed-loop system has a small bandwidth of 300 Hz.

*Remark 1:* As reported in [17], there is nonzero cross coupling between the lateral axes of the open-loop scanner, which increases from  $-20$  dB at low frequencies to about  $-5$  dB at the 10 kHz resonance. Because of the adequate

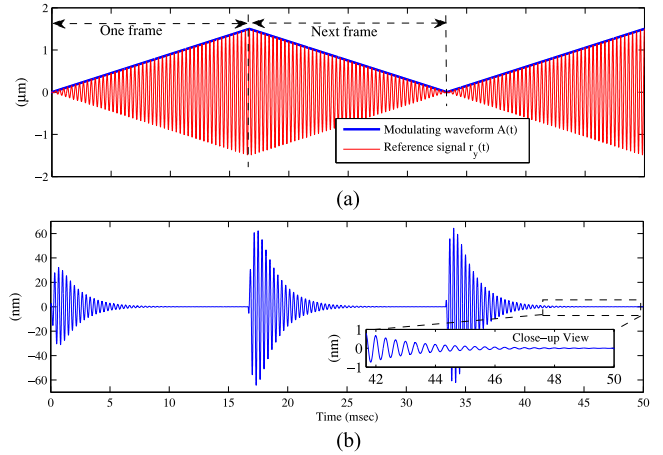


Fig. 3. (a) Selected modulating waveform and the resulting reference signal. (b) Simulated tracking error.

stability margins of the Single Input Single Output (SISO) loops, the MIMO control system is still stable when both feedback loops are implemented, simultaneously. Under these conditions, the IMC controllers provide zero cross-coupling from the references inputs to the displacement outputs, at 0, 3, 6, and 9 kHz. Otherwise, the IMC controllers would generate unbounded actuation signals in response to a stationary reference signal at those frequencies, which would contradict the stability condition. Alternatively, as shown in Fig. 1, the loop gain magnitude tends to infinity at those frequencies. Hence, the sensitivity functions become zero and provide zero cross-coupling for the closed-loop system at those frequencies.

#### IV. SPIRAL TRAJECTORY FOR SEQUENTIAL IMAGING

Conventionally, a spiral trajectory assumes a pair of sinusoidal reference signals with an identical frequency  $\omega$  and  $90^\circ$  phase difference for  $x$ - and  $y$ -axes of the scanner as

$$r_x(t) = A(t) \sin(\omega t); \quad r_y(t) = A(t) \cos(\omega t) \quad (5)$$

where the modulating waveform  $A(t)$  varies with time, linearly. To generate a video of the sample, we need to capture AFM images, sequentially. The most straightforward way of capturing successive images by spiral trajectories is to modulate the amplitude of sinusoids by a triangular waveform, which periodically varies between 0 and radius  $R$  of the scan area. Individual images are successively generated during rising and falling intervals of the triangular waveform. In each interval, the reference signal is a sinusoid multiplied by a linearly time varying signal, whose dynamics are included in the IMC of Section III if the rising or falling interval were to last, indefinitely. In other words, the dynamics of the whole reference signal contains a large number of modes, which are not completely included in the IMC. Hence, nonzero steady-state tracking errors are expected for the video-spiral references (5) even if the plant were an ideal Linear Time Invariant (LTI) system.

We can evaluate performance of the designed controller for tracking of such a video-spiral reference by simulation. Fig. 3(a) shows the selected modulating waveform  $A(t)$  along with the resulting reference signal for the  $y$ -axis. Having the frequency

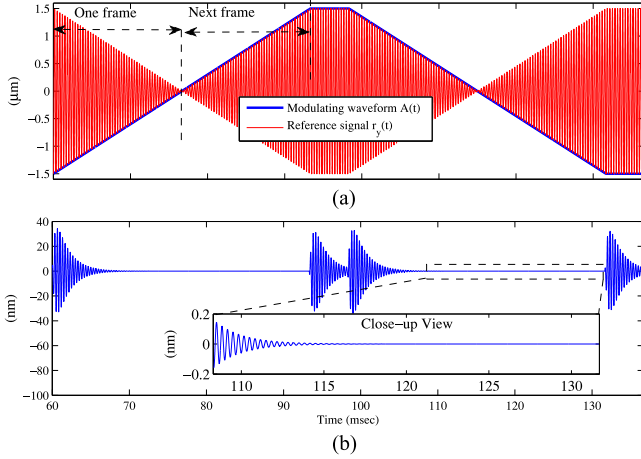


Fig. 4. (a) Selected modulating waveform and the resulting reference signal. (b) Simulated tracking error.

of sinusoids fixed at  $f = 3$  kHz and scan area diameter at  $3 \mu\text{m}$ , the slope of modulating waveform was selected so that spacing between the two adjacent scan paths in the spiral trajectory (pitch) is 30 nm. We define the resolution of a spiral trajectory as the maximum spacing between two adjacent scan lines. The 30-nm resolution was selected based on the noise level of the capacitive sensors used to measure the lateral displacements, whose standard deviations vary between 10 and 12 nm. The resulting tracking error, shown in Fig. 3(b), indicates a very desirable control performance for a video-spiral reference that corresponds to 60 frames/s (f/s). However, our objective is to further reduce the error so that the peak of tracking error does not exceed the 30 nm spiral pitch. Note that the maximum errors occur after the switching moments when the slope of the modulating waveform is changed, discontinuously.

We now examine the performance of a video-spiral reference whose modulating waveform is a trapezoidal signal that varies between  $-R$  and  $+R$ , as shown in Fig. 4(a). To have the same 30 nm pitch as before, the slopes of falling and rising intervals in the trapezoidal waveform are identical to those of the previous triangular waveform. In each interval, the modulating waveform crosses into the opposite direction, extending the duration of smooth variation of the reference signal twice without affecting the frame period (each interval contains two frames). To further reduce the level of slope discontinuity, the modulating waveform also includes time-invariant intervals between the falling and rising intervals. An inspection of the simulated tracking error in Fig. 4(b) reveals that the selected modulating waveform eliminates the error arising from frame transitions at the zero-crossings of the trapezoidal signal. In addition, the resulting peak tracking error due to slope discontinuity of the modulating waveform is almost half that of the previous case. However, it is still close to the pitch value and, hence, unacceptable. Moreover, the data obtained during the invariant intervals of the trapezoidal waveform may not be used for image generation.

### A. Smooth Video Spiral Reference

In this section, we propose a smooth spiral trajectory to further reduce the peak tracking error during sequential imaging. The

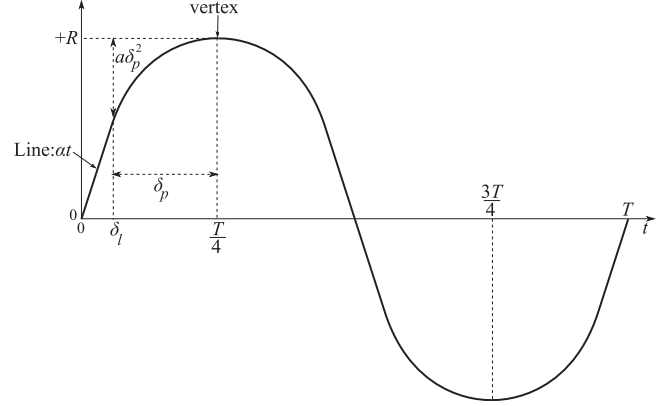


Fig. 5. Characteristics of the proposed smooth modulating waveform for the first quarter of the waveform period. The remaining three quarters are built by mirroring this curve around horizontal and vertical axes.

modulating waveform is similar to the foregoing trapezoidal waveform but the invariant intervals are replaced by parabolas to provide a smooth waveform. Fig. 5 illustrates the first quarter of one period of the waveform, which consists of two time intervals  $\delta_l$  and  $\delta_p$ , where linear and parabolic profiles are assumed, respectively. Again, we assume that the frequency of sinusoids, the dimension of the scan area, and maximum spacing between the scan curves are selected in advance. Hence, the amplitude  $R$  and slope  $\alpha$  of the linear part are known and we need to determine coefficient  $a$  of the parabolic curve as well as time intervals  $\delta_l$  and  $\delta_p$ . For a smooth transition between the linear and parabolic intervals, the slope of the parabola at  $t = \delta_l$  should be equal to that of the line

$$2a\delta_p = \alpha. \quad (6)$$

Considering the geometry in Fig. 5, the line slope  $\alpha$  is also written as  $\frac{R - a\delta_p^2}{\delta_l}$ . Applying (6) and considering the relationship between the time intervals we obtain

$$\delta_l + \frac{\delta_p}{2} = \frac{R}{\alpha}; \quad \delta_l + \delta_p = \frac{T}{4} \quad (7)$$

where  $T$  is the period of the modulating waveform. Solving for  $\delta_l$  and  $\delta_p$  in terms of the period  $T$  from the simultaneous linear equations in (7), we obtain

$$\delta_l = \frac{2R}{\alpha} - \frac{T}{4}; \quad \delta_p = \frac{T}{2} - \frac{2R}{\alpha}. \quad (8)$$

Since the time intervals are positive values, the period of the modulating waveform must be selected in the following range

$$\frac{4R}{\alpha} < T < \frac{8R}{\alpha}. \quad (9)$$

An alternative way to select the period is to first assign a positive value to the ratio of the parabolic time interval to the linear interval, defined as  $F = \frac{\delta_p}{\delta_l}$ . Then, the period is determined from (8) as

$$T = \frac{1 + F}{2 + F} \times \frac{8R}{\alpha}. \quad (10)$$

Having determined the period, the linear and parabolic time intervals are determined from (8). Having obtained  $\delta_p$ , coefficient

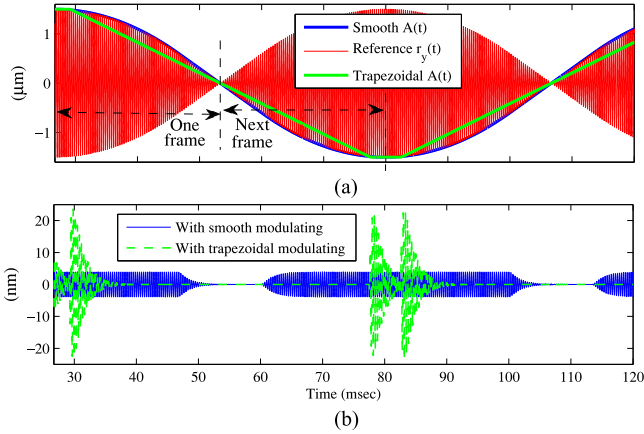


Fig. 6. (a) Selected modulating waveform and the resulting reference signal. (b) Simulated tracking error.

$a$  is determined from (6) as  $a = \alpha / (2\delta_p)$  and the parabolic time profile of the modulating waveform is determined as

$$A(t) = \begin{cases} (-1)^k \left[ R - a \left( t - \frac{T}{4} - \frac{kT}{2} \right)^2 \right], \\ (-1)^k \alpha \left( t - \frac{kT}{2} \right), \end{cases} \quad \text{if } t \in \left[ \frac{kT}{2} + \delta_l, \frac{kT}{2} + \delta_p + \frac{T}{4} \right] \quad (11)$$

$$\text{if } t \in \left[ \frac{kT}{2} - \delta_l, \frac{kT}{2} + \delta_l \right]$$

where  $k = 0, 1, 2, 3, \dots$

To examine the implications of the proposed smooth modulation waveform on the tracking error, we assume the maximum slope of  $\alpha = 90 \frac{\mu\text{m}}{\text{s}}$  and scan area radius of  $R = 1.5 \mu\text{m}$ , as before. Selecting  $F = 3$  and following the above procedure, the smooth modulating waveform is determined and can generate 37.5 f/s. The modulating waveform, reference signal, and the resulting steady-state tracking error are shown in Fig. 6. Also included in the figure are the results associated with a trapezoidal modulating waveform, with the same amplitude and period as the smooth modulating waveform. Note that the maximum magnitude of the steady-state tracking error can be reduced more than four times by applying the smooth modulating waveform instead of the trapezoidal one. This improvement is justified by the spectra of these reference signals in Fig. 7. Clearly, the amplitudes of the side frequency components in the smoothly modulated reference are significantly smaller than those in the trapezoidally modulated reference. As shown in Fig. 7(c), the closed-loop sensitivity function has a narrow rejection bandwidth around 3 kHz. Hence, the effects of the side frequency components of the smoothly modulated reference on the tracking error are attenuated more, leading to a better tracking performance.

*Remark 2:* The parabolic time profile is the minimum-order polynomial to generate a smooth modulating waveform. It also makes the synthesis procedure simpler. In addition, it guarantees that the magnitude of the tracking error remains constant during the parabolic interval, when the closed-loop system is driven by the reference. To show this, assume that the plant is LTI and the parabolic time interval lasts indefinitely. When the

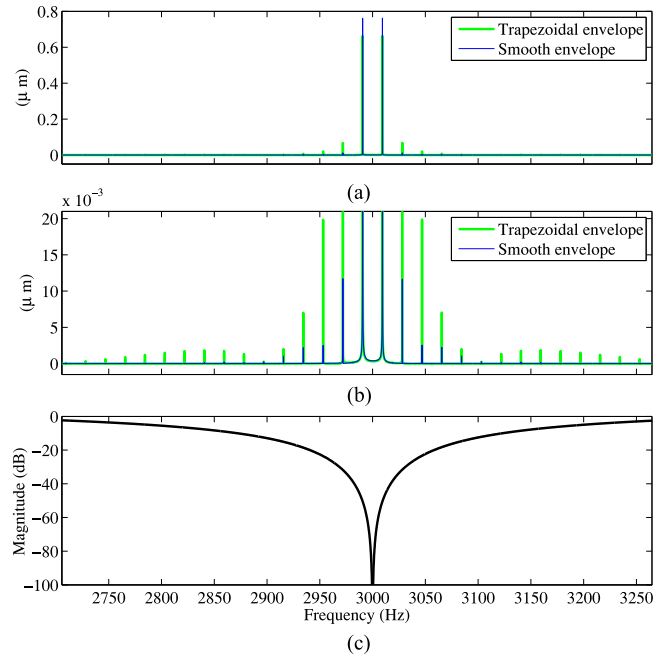


Fig. 7. (a) Fast Fourier transforms of the reference signals modulated by the trapezoidal and the smooth waveforms. (b) Close-up view of the side frequencies in Fig. 7(a). (c) Magnitude of the closed-loop sensitivity function (from the reference to the error signal  $e_y$ ) around the carrier frequency of the spiral reference.

sinusoidal signal is modulated (multiplied) by the parabolic time profile, the resulting reference signal generally contains triple imaginary pole pairs at  $\pm i\omega$ . Since the closed-loop system in Fig. 2 is stable, all signals in the loop should have pole pairs at  $\pm i\omega$ , repeated no more than three times. Considering that the controller already has two pairs of poles at  $\pm i\omega$ , the controller input signal (tracking error) cannot have more than one pair of poles at  $\pm i\omega$  (otherwise, the controller output would have more than three pairs of poles at  $\pm i\omega$ , which contradicts the stability condition). Having only one pair of poles at  $\pm i\omega$  in the tracking error, reveals that it converges to a sinusoidal signal with constant amplitude. This is also confirmed by the simulation shown in Fig. 6, during the parabolic intervals.

*Remark 3:* To generate the smooth modulating waveform whose profile in the first period is shown in Fig. 5, we used a lookup table with the data points shown in Fig. 8. The lookup table outputs the smooth waveform when it is driven by the triangular signal shown in Fig. 8. This signal can be obtained by integrating a zero-mean square wave signal with unity amplitude, 50% duty cycle, and a phase lead equal to one quarter of the period.

## B. Experimental Tracking Performance

We digitally implemented the controller (1) on the  $x$ - and  $y$ -axes of the scanner in real time with a sampling frequency of 80 kHz. To generate the spiral trajectory, we applied orthogonal sinusoidal references with time-varying amplitudes and a frequency of 3 kHz to the control systems of the two axes, simultaneously. The selected smooth modulating wave-

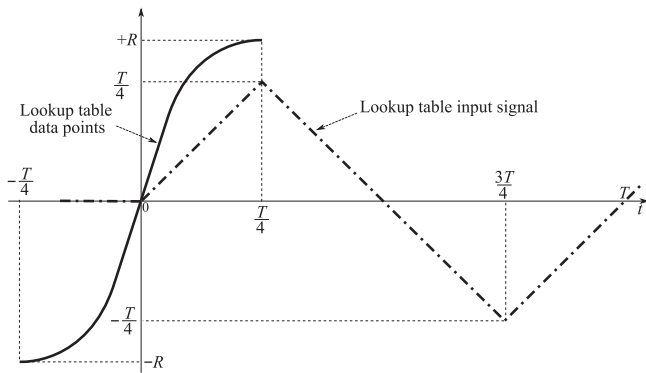


Fig. 8. Data points used in the lookup table (solid line) along with the triangular signal (dash-dot line) driving the lookup table to generate the smooth modulating waveform.

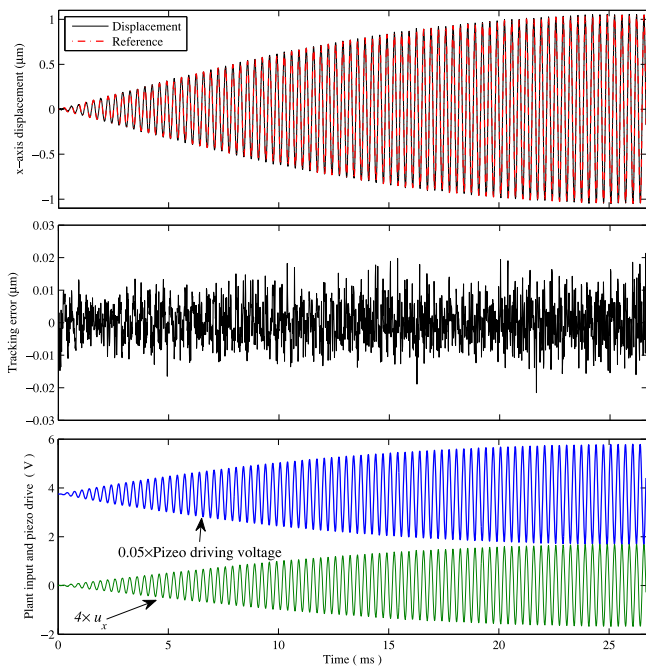


Fig. 9. Performance of the proposed control system in tracking of a spiral waveform for the  $x$ -axis. An output offset of 75 V was applied to the piezo drive amplifiers so that the nanopositioner swings around an operating point in the middle of the travel range. A similar performance was also obtained for the  $y$ -axis.

form is the same as the waveform designed in Section IV-A but the amplitude is scaled down to  $1 \mu\text{m}$ . In the Appendix, we have provided more details on experimental implementation of the controllers. Fig. 9 illustrates the tracking performance of the  $x$ -axis during an intermediate frame, which lasts only 26.7 ms and corresponds to a high frame rate of 37.5 F/S. The tracking error has a root-mean-square (rms) value of 6.1 nm, which is 0.31% of the  $2 \mu\text{m}$  scan diameter. Despite the low closed-loop bandwidth of 300 Hz, the tracking performance is remarkable for a 3 kHz spiral reference whose maximum pitch is 30 nm (indicating a high rate of amplitude variation for the

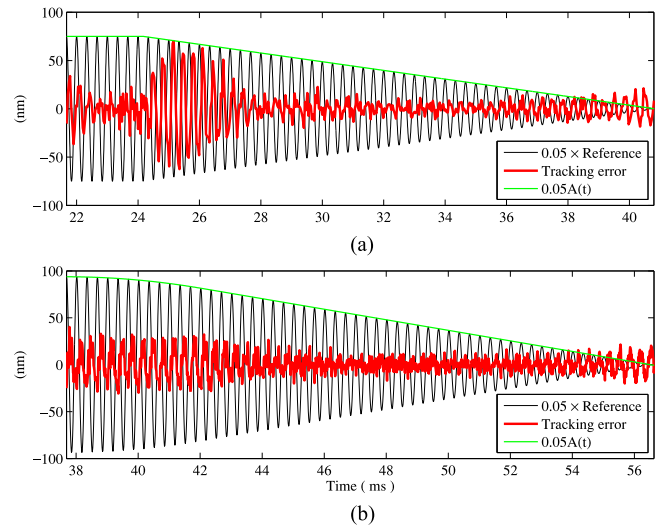


Fig. 10. Tracking error and reference signals of the  $x$ -axis during one frame of two video spiral scans with the (a) trapezoidal and (b) smooth modulating waveforms.

sinusoidal references, when the modulating signal magnitude is less than  $0.4 \mu\text{m}$ ).

We now demonstrate benefits of the smooth modulating waveform compared to the trapezoidal modulation. The experimental tracking errors obtained by the two different modulating waveforms are reported in Fig. 10. In Fig. 10(a), the video spiral reference covers a  $3\text{-}\mu\text{m}$  diameter scan area and has a 30-nm pitch generated by a trapezoidal modulating waveform. The scan area diameter and maximum pitch for the smooth video spiral reference in Fig. 10(b) are  $3.75 \mu\text{m}$  and 37.5 nm, respectively ( $\alpha = 112.5 \frac{\mu\text{m}}{\text{s}}$  and  $F = 0.3$ ). In these trapezoidal and smooth results, the rms values of the tracking errors are 16.1 and 10.7 nm, i.e., 0.54% and 0.29% of their scan diameters, respectively. The maximum magnitudes of the tracking errors are 70.2 and 40.2 nm, i.e., 2.34% and 1.07% of the scan diameter for the trapezoidal and smooth cases, respectively. In addition to the foregoing improvements, the scan area and the maximum pitch in the smooth case is 0.25% larger than the trapezoidal case.

## V. CONTROL OF CANTILEVER DEFLECTION

To obtain AFM images under a constant-force condition, the deflection of the AFM cantilever should be maintained at a constant level during the scan period. Hence, a feedback control system is required to regulate the deflection by driving the vertical piezoelectric actuators of the scanner. The  $z$ -axis actuator includes a dual-mounted structure which considerably attenuates the first resonance peak of the scanner at 20 kHz, leaving highly resonance peaks at 60 and 83 kHz [18]. To suppress the vibration of these resonance modes, an IRC compensator drives the dual-mounted actuators by piezoelectric sensor feedback and an auxiliary input voltage  $u$  [18], as illustrated in Fig. 11.

Having damped the vibration modes of the  $z$ -axis, we can implement a high-bandwidth proportional-integral (PI) controller

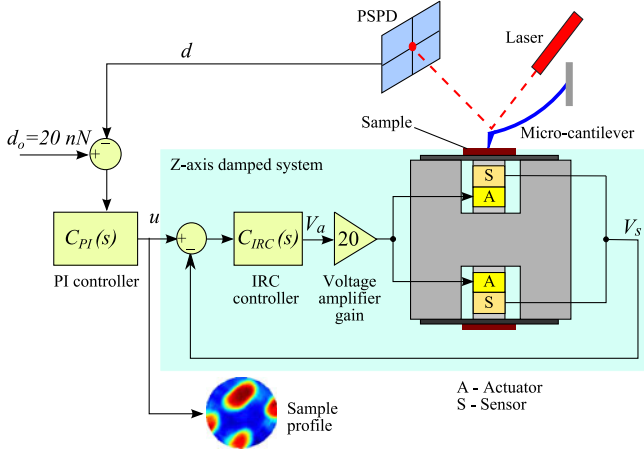


**Fig. 11.** Schematic of the  $z$ -axis feedback control strategies in constant-force contact mode. The  $z$ -axis scanner uses a dual-mounted configuration to passively suppress its first mechanical resonant peak. An IRC controller is used to suppress subsequent resonant modes [18]. The deflection of the cantilever is regulated using a PI controller.

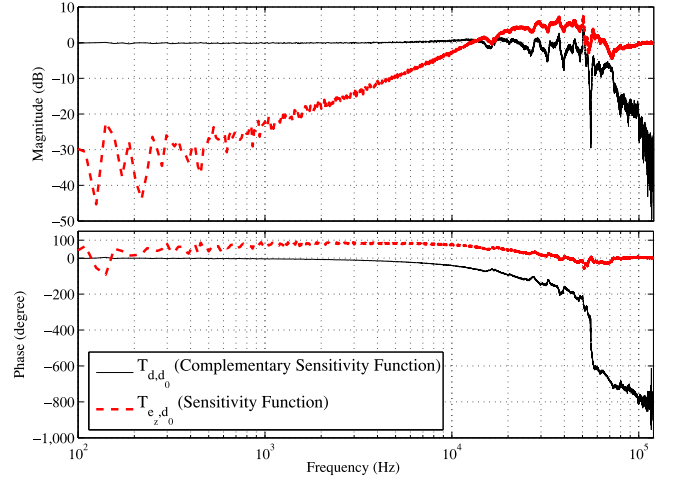


**Fig. 13.** Experimental frequency responses of the cantilever deflection and the error signal to the reference with the PI feedback loop closed on the  $z$ -axis.

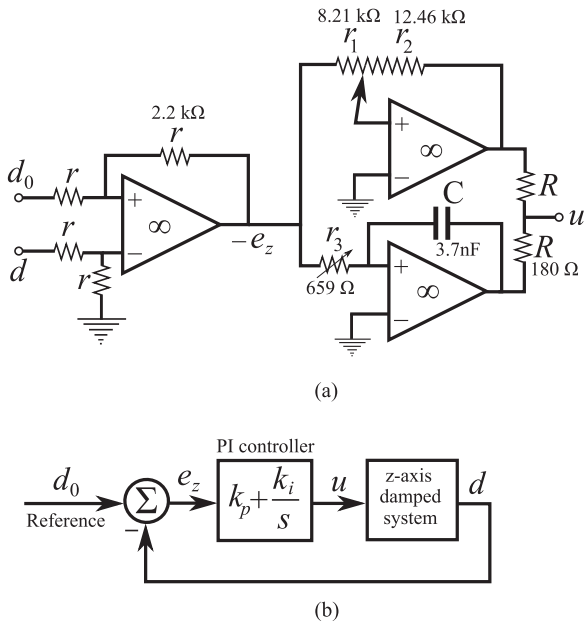


**Fig. 12.** (a) Circuit diagram of the implemented PI controller, where two potentiometers were used to tune the controller gains to maximize the closed-loop bandwidth. (b) Schematic diagram of the PI control system for regulation of the cantilever deflection.

to effectively regulate the deflection signal. Fig. 12 shows the circuit diagram used to implement the PI controller along with a schematic of the PI feedback control system. Assuming ideal op-amps and considering the low output resistance of the circuit ( $90 \Omega$ ) compared to the input resistance of the damped  $z$ -axis circuitry ( $2.2 \Omega$  [18]), the proportional and integral gains in the PI controller are obtained as

$$k_p = \frac{r_2}{2r_1} = 0.93 \quad (12)$$

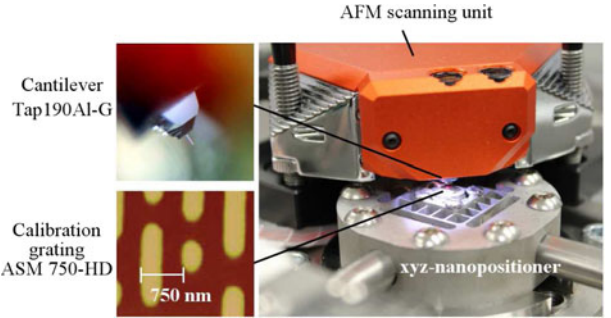


**Fig. 14.** AFM scanning unit and  $xyz$ -nanopositioner.

$$k_i = \frac{1}{2r_3C} = 2.056 \times 10^5 \left( \frac{1}{s} \right). \quad (13)$$

The experimental frequency responses of the complementary sensitivity and sensitivity functions for the PI feedback control system are shown in Fig. 13, indicating a bandwidth of 46 kHz with gain and phase margins 6.3 dB and  $62.3^\circ$ .

## VI. HIGH-SPEED AFM IMAGING

The AFM imaging performance of the closed-loop nanopositioning system discussed in Section III is evaluated here. The  $xyz$ -nanopositioner which was mounted under a Nanosurf EasyScan 2 AFM is illustrated in Fig. 14. A 190-kHz cantilever with a stiffness of 48 N/m was used to perform the scans. A calibration grating with feature height of 100 nm and pitch of 750 nm was used to evaluate the scans. The sample was mounted on the nanopositioner and spiral-scanned at 3-kHz sinusoidal inputs. The cantilever was slowly moved across the sample to spiral-scan different surface areas. Videos were captured in both constant-height and constant-force contact modes. The AFM's optical system was used to measure the deflection of the cantilever. Note that in constant-height contact mode, the tracking

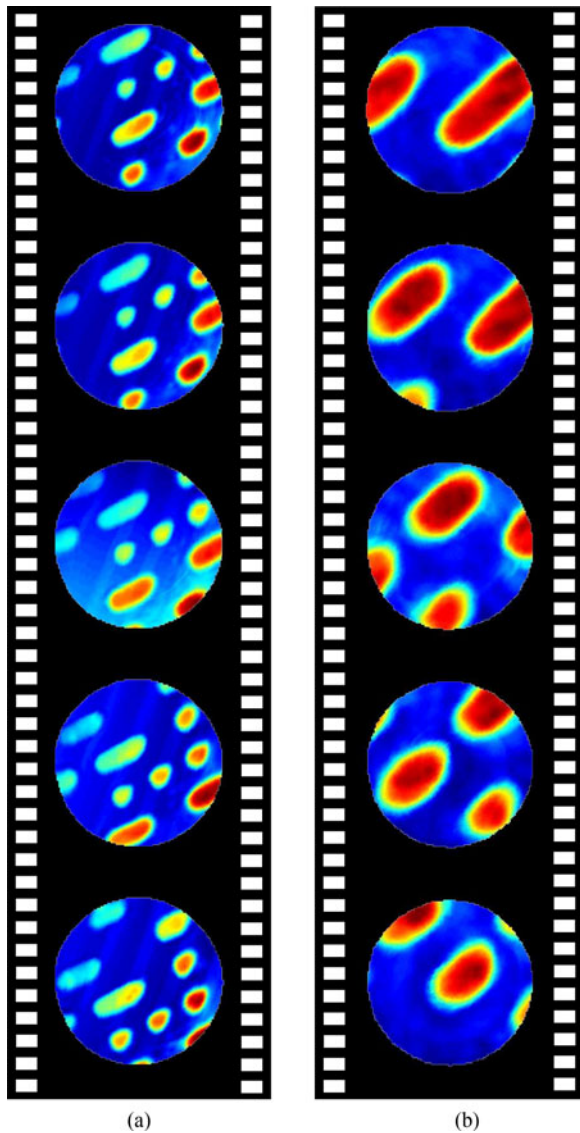


**Fig. 15.** Series of video frames showing AFM images of a slowly moving sample. Every sixth image in the series is shown above. Each frame was captured at video-rate of 37.5 F/S. (a) Constant-height contact mode: Images in a  $3\text{-}\mu\text{m}$ -diameter circular window were captured. (b) Constant-force contact mode: Images in a  $1.5\text{-}\mu\text{m}$ -diameter circular window were captured.

feedback control loop in the  $z$ -axis was turned OFF, however, the  $z$ -axis was damped using the IRC controller [18] as previously discussed to minimize vibration. The schematic of the system in this mode is similar to Fig. 11, however, the auxiliary input  $u$  is set to zero and the sample height profile is obtained from the deflection signal  $d(t)$ , while the cantilever base is held stationary.

In constant-force contact mode, the vertical feedback control strategies as discussed in Section V were used to replace the AFM's vertical feedback loop. The contact force was regulated at 20 nN during the scans. The schematic of the AFM system in this mode is shown in Fig. 11, where topographical information is extracted from the manipulated auxiliary input  $u$ .

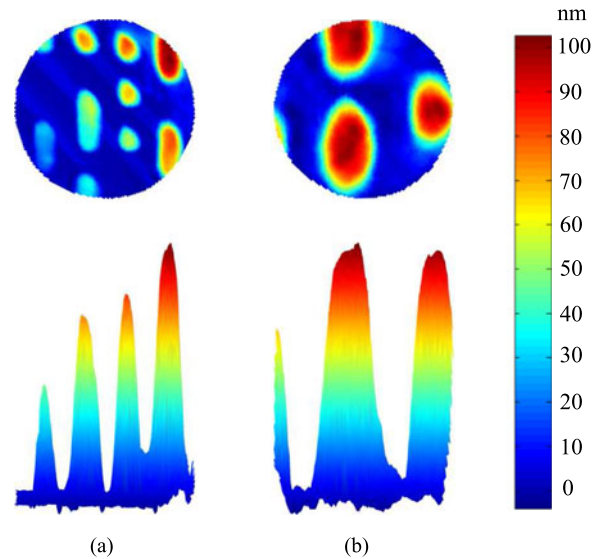


**Fig. 16.** Profile height of images captured in (a) constant-height contact mode and (b) constant-force contact mode.

Fig. 15(a) shows a series of closed-loop spiral images captured at video-rate 37.5 F/S in constant-height contact mode. The diameter of the images is  $3\text{ }\mu\text{m}$ . The proposed control method eliminates image artifacts associated with vibration and poor lateral tracking during video-rate AFM scanning. However, some of the features start to disappear as the cantilever moves across the surface area of the sample. The gradually reduced profile height can be observed from the side view of an image as illustrated in Fig. 16(a). This is due to the slight tilt of the sample relative to the  $xy$ -plane of the cantilever. When the cantilever moves across the sample, the increasing distance between cantilever and sample leads to insufficient contact force between the two. Without vertical feedback control to regulate the cantilever deflection and, hence, the contact force, topographical information of some features were lost during the high-speed scans.

Closed-loop spiral images captured at 37.5 F/S in constant-force contact mode are illustrated in Fig. 15(b). Note that the image size was reduced to  $1.5\text{ }\mu\text{m}$ -diameter due to the limited bandwidth of the vertical axis. The proposed spiral trajectory and control strategies eliminate image artifacts associated with poor tracking and vibration. Furthermore, the frame quality is substantially improved by regulating the contact force, thus avoiding the loss of topographical information during video-speed scans. Consistent feature height can be seen in Fig. 16(b). Artifact-free property of the resulting images is further revealed by comparison with the image of the same sample obtained by a 100-Hz sinusoidal scan in constant-force mode [18], where the maximum lateral velocity is nine times smaller.

Fig. 17 shows a time interval of the regulated deflection error signal  $e_z$  in nm along with the corresponding sample height from the control signal  $u$  in the constant-force mode, indicating the desirable control performance of the PI feedback system in maintaining small cantilever fluctuations (less than 2.5 nm)

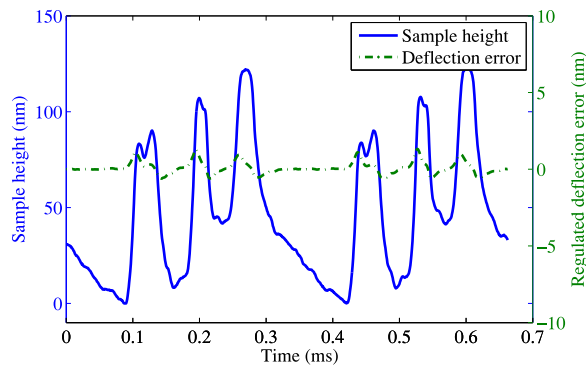


Fig. 17. Profile height and regulated cantilever deflection.

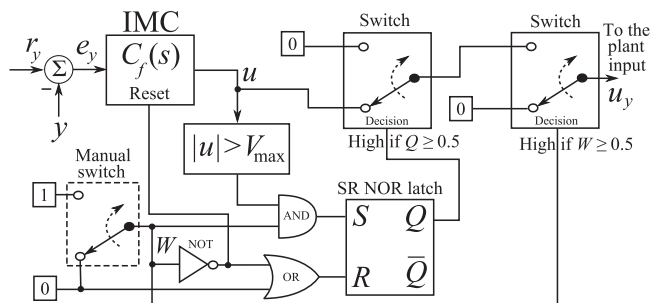


Fig. 18. Schematic of the switching mechanism used for the  $y$ -axis control system. The manual switch is used to close the loop. The logic circuit is used to ground the plant input if the controller output exceeds  $V_{max}$  at any instant, while the manual switch is on (the state of RS flip-flop (latch) is not changed if its inputs are held at zero).

while sample features as high as 100 nm hit the cantilever tip, periodically. The raw sample height signal in Fig. 17 includes an intrinsic periodic signal with the same fundamental frequency as the sinusoids (3 kHz), which is due to the nonzero tilt of the sample plane. This tilt signal, which does not carry useful feature data of the sample, has been approximately canceled in all topographical AFM images presented in Figs. 15 and 16.

## VII. CONCLUSION

An IMC was designed to track a spiral trajectory with a specific carrier frequency. We incorporated repeated purely imaginary poles at the carrier frequency into the controller, in addition to an integrator and imaginary poles at the second and third harmonics of the carrier frequency to cancel effects of dominant plant nonlinearities, such as piezoelectric hysteresis and creep. With a limited closed-loop bandwidth of 300 Hz along the lateral axes, we accurately tracked a high-pitch spiral trajectory with 3-kHz carrier frequency to capture high-rate AFM images. A smooth waveform was proposed for amplitude modulation of the sinusoids generating the spiral pattern to considerably reduce the tracking error during sequential imaging. A synthesis procedure was developed to determine the waveform parameters based on prespecified values for the scan area diameter, image resolution, and carrier frequency. By implementing a high-bandwidth analogue PI controller on the damped  $z$ -axis

of the nanopositioner to regulate the cantilever deflection, we achieved constant-force AFM images at an ultravideo frame rate of 37.5 F/S.

## APPENDIX

We applied a practical method for controller implementation and tuning. Since the IMC controller includes undamped poles, it can generate signals with linearly growing amplitudes, if the loop is left open. In addition, during the tuning of controller parameters, the closed-loop system may become unstable. Hence, it is desirable to design a switching mechanism to close and open the loop, appropriately. To address these problems, we used transfer functions equipped with external reset inputs to ensure the controller output is zero when the feedback loop is closed. We also protected the plant from unstable signals by a switch that permanently grounds the plant input, if the controller output exceeds a certain level ( $V_{max}$ ) at any instant after closing the loop. Fig. 18 illustrates the switching system we used for the  $y$ -axis control system.

## REFERENCES

- [1] T. Ando, "High-speed atomic force microscopy coming of age," *Nanotechnology*, vol. 23, no. 6, 2012, Art. no. 062001.
- [2] G. M. Whitesides and J. C. Love, "The art of building small," *Sci. Amer.*, vol. 285, no. 3, pp. 32–41, 2001.
- [3] B. Bhushan, *Handbook of Micro/Nanotribology*, 2nd ed. Boca Raton, FL, USA: CRC Press, 1999.
- [4] Y. K. Yong, S. O. R. Moheimani, B. J. Kenton, and K. K. Leang, "Invited review article: High-speed flexure-guided nanopositioning: Mechanical design and control issues," *Rev. Sci. Instrum.*, vol. 83, no. 12, 2012, Art. no. 121101.
- [5] Y. K. Yong, S. Aphale, and S. O. R. Moheimani, "Design, identification and control of a flexure-based XY stage for fast nanoscale positioning," *IEEE Trans. Nanotechnol.*, vol. 8, no. 1, pp. 46–54, Jan. 2009.
- [6] Y. K. Yong, A. Bazaee, and S. O. R. Moheimani, "Video-rate Lissajous-scan atomic force microscopy," *IEEE Trans. Nanotechnol.*, vol. 13, no. 1, pp. 85–93, Jan. 2014.
- [7] S. O. R. Moheimani, "Invited Review Article: Accurate and Fast Nanopositioning with Piezoelectric Tube Scanners: Emerging Trends and Future Challenges," *Rev. Sci. Instrum.*, vol. 79, no. 7, 2008, Art. no. 071101.
- [8] Y. K. Yong, S. O. R. Moheimani, and I. R. Petersen, "High-speed cycloid-scan atomic force microscopy," *Nanotechnology*, vol. 21, no. 36, 2010, Art. no. 365503.
- [9] A. Bazaee, Y. K. Yong, and S. O. R. Moheimani, "High-speed Lissajous-scan atomic force microscopy: Scan pattern planning and control design issues," *Rev. Sci. Instrum.*, vol. 83, no. 6, 2012, Art. no. 063701.
- [10] T. Tuma, J. Lygeros, V. Kartik, A. Sebastian, and A. Pantazi, "High-speed multiresolution scanning probe microscopy based on Lissajous scan trajectories," *Nanotechnology*, vol. 23, no. 18, 2012, Art. no. 185501.
- [11] I. A. Mahmood, S. O. R. Moheimani, and B. Bhikkaji, "A new scanning method for fast atomic force microscopy," *IEEE Trans. Nanotechnol.*, vol. 10, no. 2, pp. 203–216, Mar. 2011.
- [12] B. Bhikkaji, M. Ratnam, A. J. Fleming, and S. O. R. Moheimani, "High-performance control of piezoelectric tube scanners," *IEEE Trans. Control Syst. Technol.*, vol. 15, no. 5, pp. 853–866, Oct. 2007.
- [13] M. Rana, H. Pota, and I. Petersen, "Spiral scanning with improved control for faster imaging of AFM," *IEEE Trans. Nanotechnol.*, vol. 13, no. 3, pp. 541–550, May 2014.
- [14] H. Habibullah, H. R. Pota, and I. R. Petersen, "High-speed spiral imaging technique for an atomic force microscope using a linear quadratic Gaussian controller," *Rev. Sci. Instrum.*, vol. 85, no. 3, 2014, Art. no. 033706. [Online]. Available: <http://dx.doi.org/10.1063/1.4868249>
- [15] H. Habibullah, H. Pota, and I. R. Petersen, "Phase-locked loop-based proportional integral control for spiral scanning in an atomic force microscope," in *Proc. 19th IFAC World Congr.*, Aug. 2014, pp. 6563–6568.
- [16] B. A. Francis and W. M. Wonham, "The internal model principle of control theory," *Automatica*, vol. 12, pp. 457–465, 1976.

- [17] Y. K. Yong, B. Bhikkaji, and S. O. R. Moheimani, "Design, modeling and FPAA-based control of a high-speed atomic force microscope nanopositioner," *IEEE/ASME Trans. Mechatronics*, vol. 18, no. 3, pp. 1060–1071, Jun. 2013.
- [18] Y. K. Yong and S. O. R. Moheimani, "Collocated Z-axis control of a high-speed nanopositioner for video-rate atomic force microscopy," *IEEE Trans. Nanotechnol.*, vol. 14, no. 2, pp. 338–345, Mar. 2015.
- [19] S. Devasia, E. Eleftheriou, and S. O. R. Moheimani, "A survey of control issues in nanopositioning," *IEEE Trans. Control Syst. Technol.*, vol. 15, no. 5, pp. 802–823, Sep. 2007.
- [20] Y. K. Yong and S. O. R. Moheimani, "Design of an inertially counterbalanced z-nanopositioner for high-speed atomic force microscopy," *IEEE/ASME Trans. Nanotechnol.*, vol. 12, no. 2, pp. 137–145, Mar. 2013.



**Ali Bazaie** (M'10) received the B.Sc. and M.Sc. degrees from Shiraz University, Shiraz, Iran; a completed Ph.D. requirement from Tarbiat Modares University, Tehran, Iran; and the Ph.D. degree from the University of Western Ontario, London, ON, Canada, in 1992, 1995, 2004, and 2009, respectively, all in electrical engineering.

From September 1995 to January 2000, he was an Instructor at Yazd University, Yazd, Iran. From September 2004 to December 2005, he was a Research Assistant in the Department of

Electrical and Computer Engineering, University of Western Ontario. Since 2009, he held a Post-Doctoral Research Fellowship and casual academic positions with the School of Electrical Engineering and Computer Science, University of Newcastle, Australia. His research interests include the general area of nonlinear systems including control and modeling of structurally flexible systems, friction modeling and compensation, neural networks, and microposition sensors. He is the author of more than 50 peer-reviewed articles, including in the *IEEE TRANSACTIONS ON AUTOMATIC CONTROL*, *Automatica*, *Systems and Control Letters*, the *ASME Journal of Dynamic Systems Measurement and Control*, the *Journal of Vibration and Control*, the *IEEE/ASME JOURNAL OF MICROELECTROMECHANICAL SYSTEMS*, the *IEEE TRANSACTIONS ON NANOTECHNOLOGY*, the *IEEE SENSORS JOURNAL*, the *IEEE/ASME TRANSACTIONS ON MECHATRONICS*, and *Review of Scientific Instruments*. He has been elected as a Future Science Leader to foster research collaborations between Australia and China through 2015 Australia China Young Scientists Exchange Program.



**Yuen Kuan Yong** (M'09) received the B.Eng. degree (First Class Hons.) in mechatronic engineering and the Ph.D. degree in mechanical engineering from the University of Adelaide, Adelaide, SA, Australia, in 2001 and 2007, respectively.

She is currently an Australian Research Council Discovery Early Career Researcher Award (DECRA) Fellow with the School of Electrical Engineering and Computer Science, University of Newcastle, Callaghan, NSW, Australia.

Her research interests include the design and control of nanopositioning systems, high-speed atomic force microscopy, finite-element analysis of smart materials and structures, sensing and actuation, and design and control of miniature robots.

Dr. Yong received the 2008 IEEE/ASME International Conference on Advanced Intelligent Mechatronics Best Conference Paper Finalist Award, the University of Newcastle Vice-Chancellor's Awards for Research Excellence, and the Pro Vice-Chancellor's Award for Excellence in Research Performance. She is an Associate Editor of *Frontiers in Mechanical Engineering* (specialty section Mechatronics) and the *International Journal of Advanced Robotic Systems*. She is also a Steering Committee Member for the 2016 International Conference on Manipulation, Automation, and Robotics at Small Scales.



**S. O. Reza Moheimani** (F'11) currently holds the James Von Ehr Distinguished Chair in Science and Technology in the Department of Mechanical Engineering, University of Texas at Dallas, Richardson, TX, USA. His current research interests include ultrahigh-precision mechatronic systems, with particular emphasis on dynamics and control at the nanometer scale, including applications of control and estimation in nanopositioning systems for high-speed scanning probe microscopy and nanomanufacturing, modeling

and control of microcantilever-based devices, control of microactuators in microelectromechanical systems, and design, modeling, and control of micromachined nanopositioners for on-chip scanning probe microscopy.

Dr. Moheimani is a fellow of the International Federation of Automatic Control (IFAC) and the Institute of Physics, U.K. His research has been recognized with a number of awards, including IFAC Nathaniel B. Nichols Medal (2014), the IFAC Mechatronic Systems Award (2013), the IEEE Control Systems Technology Award (2009), the IEEE TRANSACTIONS ON CONTROL SYSTEMS TECHNOLOGY Outstanding Paper Award (2007), and several best paper awards from various conferences. He is the Editor-in-Chief of *Mechatronics* and has served on the editorial boards of a number of other journals, including the *IEEE/ASME TRANSACTIONS ON MECHATRONICS*, the *IEEE TRANSACTIONS ON CONTROL SYSTEMS TECHNOLOGY*, and *Control Engineering Practice*. He currently chairs the IFAC Technical Committee on Mechatronic Systems, and has chaired several international conferences and workshops.